

Cite this: DOI: 00.0000/xxxxxxxxxx

Automated Routing of Droplets for DNA Storage on a Digital Microfluidics Platform

Ajay Manicka, Andrew Stephan, Sriram Chari, Gemma Mendonsa, Peyton Okubo, John Stolzberg-Schray, Anil Reddy, and Marc Riedel

Received Date
Accepted Date

DOI: 00.0000/xxxxxxxxxx

Technologies for sequencing (reading) and synthesizing (writing) DNA have progressed on a Moore's law-like trajectory over the last three decades. This has motivated the idea of using DNA for data storage. Theoretically, DNA-based storage systems could out-compete all existing forms of archival storage. However, a large gap exists between what is theoretically possible in terms of read and write speeds and what has been practically demonstrated with DNA. This paper introduces a novel approach to DNA storage, with automated assembly on a digital microfluidic biochip. This technology offers unprecedented parallelism in DNA assembly using a dual library of "symbols" and "linkers". An algorithmic solution is discussed for the problem of managing droplet "traffic" on the digital microfluidic device, with prioritized A star routing. Detailed simulation results are presented for routing a large number of droplets in parallel on the device, minimizing the amount of congestion, and maximizing throughput.

1 Introduction

1.1 The World of Information

The amount of data that the world generates has been increasing exponentially since the inception of the computer age. This trend will continue for the foreseeable future, as ever more IoT devices come online and as humans create ever denser content in the form of video and virtual reality. The bulk of this so-called "big data" is stored in hard disk drives (HDDs)¹. It is estimated that total demand for data storage by 2025 will be 180 zettabytes (1 zettabyte = 1 billion terabytes)², which would be a three fold increase from 2020. Some of this newly generated data will need to be archived for long-term storage. Even if only 5% of stored data is placed in "deep" offline archives, this would require 30 million 20TB HDDs by 2025³. Online and on-premise archive capacities will be many times larger. Meanwhile, with respect to storage media supply, it is projected that the installed base will grow less than 20% year over year in the same time-frame⁴. Without construction of new HDD and SSD manufacturing facilities, which are multi-billion dollar investments, demand for storage is expected to outstrip supply by as much as two-fold⁵. Furthermore, mag-

netic storage has durability limitations that make it undesirable for maintenance-free, multi-decade storage. Also, the proliferation of data centers is causing long-term environmental damage, as the electricity they require (mostly for cooling) is a major source of global carbon emissions⁶. For all these reasons, there has been a strong interest in identifying new types of storage media.

A strong contender for a type of media that could meet the future demand for archival storage is DNA. The theoretical storage capacity of DNA is as high 200 petabytes per gram (around 800 times denser than modern hard drives)⁷. Most importantly, the energy requirement for writing is on the order of 10^{-19} joules per bit which is orders of magnitude below the femtojoules/bit (10^{-15} joules per bit) barrier touted for other emerging technologies⁸. The durability of DNA is unmatched, exceeding centuries, while hard drives and magnetic tape rarely maintain reliability longer than 30 years⁹. We point to a review paper that summarizes the potential of DNA storage systems¹⁰.

1.2 DNA as a Storage Unit

Traditional computer systems use the binary code of zeros and ones $\{0, 1\}$ as storage units. In its simplest form, a DNA storage system uses a quaternary code of nucleotides drawn from four different nitrogenous bases, viz. adenine, guanine, cytosine, and thymine, denoted $\{A, G, C, T\}$ respectively. We can map couplets of zeros or ones directly to each nucleotide, as illustrated in Fig. 1. In this way, we use a string of nucleotides to represent arbitrary data.

With such an encoding, a DNA sequence with n nucleotides stores $2n$ bits of data based on binary mapping (see Fig. 1). Table 1 introduces our concept of a DNA Symbol library.* We note here that certain terms will be defined in footnotes in the following text. From a base set of the 4 nucleotides $\{A, G, C, T\}$,

* A DNA Symbol library is a set of nucleotide sequences of length n , which we can use as building blocks to assemble large chains of DNA.



Fig. 1 This figure represents the mapping of nucleotide bases to a binary code. Just as we can string together binary values, we can assemble DNA nucleotides chemically to represent data.

there are 16 ways to select base pairs of length 2; these base pair symbols correspond to binary numbers from 0000 to 1111. If a 2-nucleotide symbol can represent 16 distinct binary numbers, then a 3-nucleotide symbol can represent 64 binary distinct numbers. In general, the addition of each nucleotide quadruples the range of numbers we can represent. So n base pairs can represent 4^n distinct numbers for $n > 0$

Table 1 DNA Symbol Library size based on Symbol Length.

Symbol Length (Number of base pairs per symbol)	DNA Symbol Library Size (Number of Unique Symbols)
1	4
2	16
3	64
4	256
5	1024
6	4096
7	16384
8	65536

Ever since Watson and Crick first described the molecular double helix structure of DNA¹¹, its potential for storage has been apparent to computer scientists. It seems that most practical work is based on liquid-handling robotics. The power consumption of liquid-handling DNA storage systems is on the order of *hundreds* of joules/sec¹⁰ for a DNA synthesis rate on the order of kilobytes/sec. Overall, these machines use a substantial amount of energy for limited gain. Many creative ideas and novel technologies, ranging from nanopores¹² to DNA origami¹³, are also being investigated. The leading approach appears to be phosphoramidite chemistry¹⁴.

The main barrier to building DNA storage systems that can compete with existing forms of archival storage are the *write* speeds, so the rate of DNA synthesis. Hard drive write speeds vary between 50 and 120 Megabytes per second, while solid-state storage systems achieve write speeds of 200 Megabytes per second¹⁵. All existing DNA storage systems have write speeds many magnitudes slower than this¹⁶.

1.3 A Solution: Increasing Rate of DNA Synthesis

Achieving practically useful write speeds will require two things. First, a way to introduce massive parallelization. Second, a chemical protocol that writes as much data as possible per operation,

thereby increasing the bitrate (write speed in bits per unit time). This paper proposes a solution to the '*synthesis-speed*' problem with a dual library of "symbols"[†] and "linkers"[‡]. The two libraries work in tandem to allow synthesis of one long gene[§] in the desired order. Since these symbols and linkers can be connected in parallel, massive parallelization is possible. This is in contrast to most existing schemes for DNA storage, in which each operation attaches a single nucleotide to the end of the sequence, for instance with phosphoramidite chemistry¹⁷.

Instead of liquid-handling robots, we perform assembly of DNA with a digital microfluidic biochip (DMFB). This technology offers the advantages of low reagent consumption, high precision, and miniaturization¹⁸. Details are discussed in Section 2.1 below. A DMFB device can be idealized as a 2-D grid, shown in Fig. 2. Most of the 2-D grid serves to route individual droplets. In our device, a subset of the available grid points performs dedicated operations: Gibson assembly (*concatenation*)¹⁹; polymerase chain reaction, or PCR (*replication*)²⁰; and purification (*correction*). One edge of the biochip houses DNA in the form of short strands called *symbols*, and the other side holds short sequences called *linkers*. On one of the edges, PCR stations are located where multiple copies of depleted DNA symbols and linkers can be created through PCR. Also, Gibson sites (locations where symbols are linked together) and purification sites are strategically positioned on the DMFB to ensure droplets can reach these desired regions.

To create a DNA-filled droplet, a single oligo[¶] is placed in a droplet which is pulled from a reservoir located on the edge of the grid. When a symbol droplet and a linker droplet merge, they form a larger droplet with the two corresponding oligos. The resulting droplet is merged with a droplet containing the necessary enzymes for Gibson assembly. Finally, the resulting droplet is routed to a station for Gibson assembly: this is where the symbol and linker oligo are chemically joined to form a single DNA strand.

The task of writing DNA begins with an encoding of the data in a gene. When the order to assemble a certain gene is received by the DMFB device, the system dispenses the requisite DNA symbols, linkers, and chemical reagents as individual droplets along the grid's edge. Each DNA or chemical-filled droplet is routed automatically to a certain site, where it is either merged with another droplet or undergoes a chemical reaction.

Routing all the droplets is a significant challenge, one that we confront in this paper. The routing problem becomes more complex as more droplets are pulled to assemble longer genes. To solve the problem of routing droplets in our DNA storage system, we use an algorithm called 3-D prioritized A*^{||}. The algorithm

[†] A **symbol** is short double-stranded sequence of DNA whose nucleotides specify the data that is being stored.

[‡] A **Linker** is a double-sided nucleotide sequence that connects two symbols together in the correct order.

[§] A **gene** is a unit of storage consists of a sequence of symbols, joined by linkers. It is the full length of DNA that is produced by the DMFB device.

[¶] An **oligo** is a relatively short sequence of nucleotides.

^{||} **3-D prioritized A*** was selected as the routing algorithm of choice because it is a complete²¹ and optimal²² heuristic based algorithm that is guaranteed to find the shortest route between a start and goal point, even in the presence of obstacles.²³

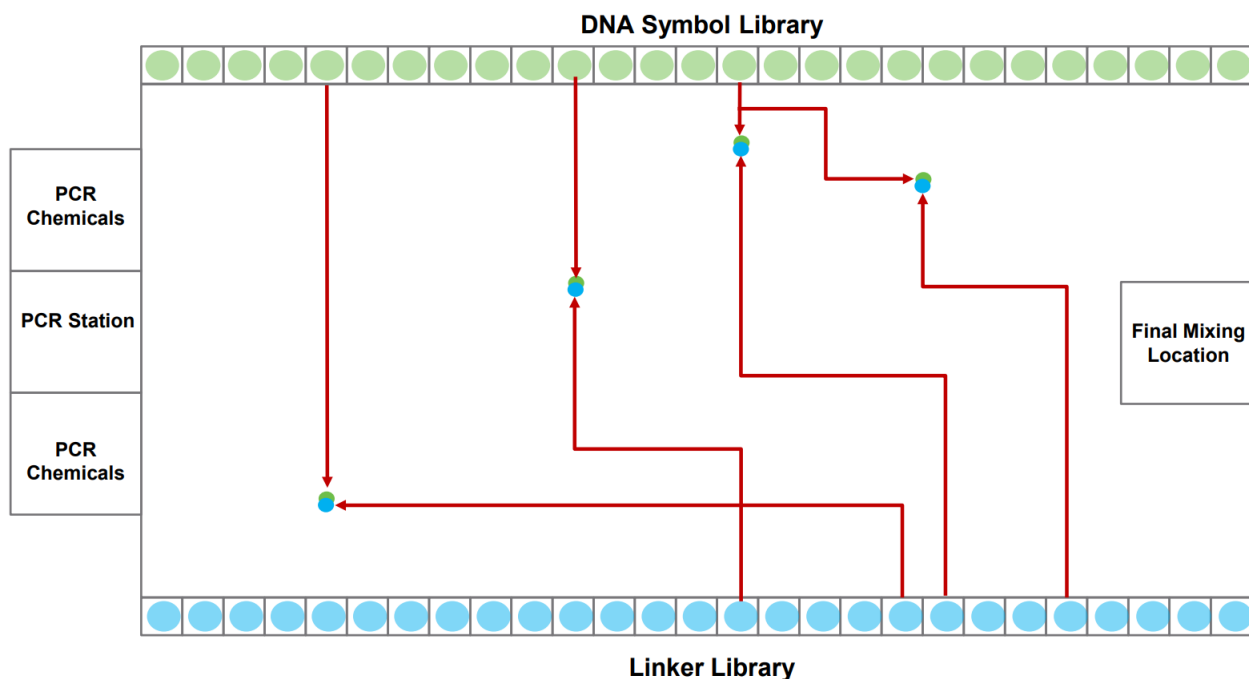


Fig. 2 A high-level visual of a digital microfluidic biochip (DMFB). Two sides contain the DNA oligos representing symbols and linkers. The other two sides contain Gibson, PCR, and "Purify" sites, along with the chemicals necessary to complete each chemical process. The figure illustrates the path that 8 droplets take, each containing a symbol or a linker. Each symbol meets up with a linker, merging into a larger droplet. The resulting droplets will then be routed to a Gibson site, where they are assembled into a longer strand.

considers three dimensions: the horizontal axis of the DMFB grid, the vertical axis of the DMFB grid, and the axis of time. It is called *prioritized* because it chooses to create routes for droplets by giving priority to the droplet which is furthest from its goal node i.e. the droplet which has to travel the largest distance across the grid to reach its intended target location. The implementation of A^* is simple and accomplishes the goal of routing droplets accurately. This heuristic based algorithm allows many droplets to move simultaneously while avoiding unwanted collisions. It also allows individual droplets to take the optimal path within the constraints given to it by higher priority droplets.

1.4 Related Work

DNA storage technology is a rapidly expanding area of research. Here we reference relevant literature describing efforts in DNA storage^{8,16,24–27}. Our approach towards DNA storage differs in the use of DMF technology and a novel "symbol" and "linker" dual library.

With respect to the routing algorithm we present, this paper builds upon an extensive body of prior work. Numerous papers have discussed routing on DMFB devices, for a variety of applications^{28–30}. More recent papers discuss using DMFB technology for DNA sequencing and clinical diagnosis for its precise movements^{31–33}. DNA storage presents very different constraints, particularly with respect to the size of the grid and the degree of parallelism. Here, we summarize the most relevant related work regarding routing on DMFBs.

A recent paper discusses routing "flexible" droplets which take different shapes³⁴. However, this is only possible using an "ac-

tive matrix" (AM) architecture which provides very different constraints. Another presents an evolutionary multi-objective optimization algorithm; it cannot guarantee that it will generate feasible path solutions for all droplets³⁵. Moreover, the algorithm has only been tested on very small grid sizes: none were greater than 50×50 . Our target size is a grid with approximately one million spaces (1000 by 1000). For this size, algorithmic runtime is a concern.

Another recent paper addresses the problem of electrode degradation using Deep Reinforcement Learning to adapt droplet routing on DMFBs³⁶. Physical DMFBs undergo electrode degradation when excess charge begins to build in the dielectric layer³⁷. This degradation would constrain the movement of droplets, which would cause unwanted collisions and stalls. Using reinforcement learning algorithms in this context takes advantage of adapting its behavior based off information learned in the previous routing iterations. This has been shown to work at a small scale on grids less than 50×50 in size. Our target size of 1000 by 1000 is much greater.

A recent paper investigates the use of a multi-commodity network flow based routing algorithm for paper-based DMFBs³⁸. The algorithm being more effective than existing routing algorithms on Paper DMFBs, we are using a metal DMFB with electrodes which are not printed on paper by an inkjet printer. Therefore, a decision was made to use a form of A^* because A^* has been used to route droplets on a DMFB in previous works, and has been shown to be effective by being complete and choosing the optimal path yet comes with the drawback of having a large time complexity^{28,39,40}. In future work, we plan to modify our

algorithm to improve routing speed, and our system’s modularity makes such a change simple to implement. However, the purpose of this paper is to introduce our system for DNA storage via automated DNA assembly, and the ease of implementing 3-D Prioritized A* made this a judicious choice for routing droplet traffic in our circumstance.

The contents of this paper are organized as follows. First, in Section 2 we describe relevant background information to explain the processes and terminology used in our system. Next, in Section 3 we describe our method of automating DNA assembly by strategically routing droplets across a DMFB. After explaining our routing scheme, we present our architectural system used to assemble DNA storage genes from start to finish. We then present simulation results using this architecture regarding runtime and memory usage. We then conclude with a summary of experimental results and discuss areas for future work.

2 Background

2.1 Digital Microfluidics (DMF) Technology

DMF is a fluid-handling technology that precisely manipulates small droplets on a grid through moving electrical charge. It works on the principle of *electrowetting*^{**}. Aqueous droplets naturally bead-up on a hydrophobic surface, but a voltage applied between a droplet and an insulated electrode can cause the droplet to spread out on the surface, as shown in Fig. 3.

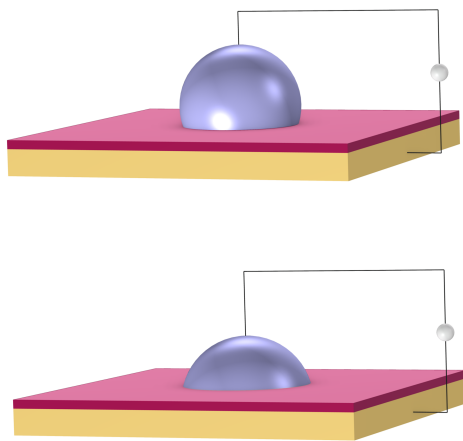


Fig. 3 Electrowetting: aqueous droplets spread applied between a droplet and an insulating electrode (shown in orange). The droplet rests upon a hydrophobic dielectric (shown in red). Top: no voltage. Bottom: high voltage.

Electrowetting allows the precise manipulation of aqueous droplets. Electrical signals are applied to an array of electrodes to define the size and position of each droplet. Droplets are moved by turning the voltage on and off in succession across adjacent electrodes. The same mechanism can be used to dispense, merge, and mix droplets using electrical signals. These basic operations become the building blocks to perform biochemical reactions.

Chemical lab work effectively becomes electronic hardware.

DMF technology itself has been studied extensively in academia⁴². In recent years, it has been applied for specific tasks in industry⁴³. However, it remains a niche technology. Scaling down the size of the electronic grid in a DMF device can be an expensive proposition⁴⁴. However, we contrast DMF with other forms of technology for chemical lab work, such as liquid-handling robotics⁴⁵. Such systems have precise servo and stepper motors to move liquid between wells. Although very capable, such systems require precision engineering. This equipment is expensive to build, maintain, and operate in terms of energy and cost. DMF technology provides lower droplet volume requirements, reduced costs, and liquid handling flexibility compared to technology like liquid-handling robotics⁴⁶. Therefore, a DMFB is used in our efforts to automate DNA assembly for storage applications.

2.2 Gibson Assembly Protocol

New possibilities arise when we assemble DNA in fragments instead of individual nucleotides. In 2009, Gibson et al. proposed a method for joining multiple DNA fragments in a single reaction⁴⁷. These fragments must have overlapping ends of several base pairs in length. In addition to the fragments to be assembled, three enzymes are also required: exonuclease, DNA polymerase, and DNA ligase. Using these enzymes, Gibson assembly can connect two double sided strands of DNA together. This Gibson assembly is general-purpose, but with some additions it can be adapted to serve as a method of constructing long data-storage strands or genes⁴⁸. A visualization of the Gibson assembly process can be seen in Fig. 4.

In the context of the DMFB, we place a symbol, linker, and three enzymes into three different droplets. These droplets are all routed to a singular Gibson site. At this location, Gibson assembly will be performed to form a larger droplet containing a singular combined symbol and linker DNA storage gene.

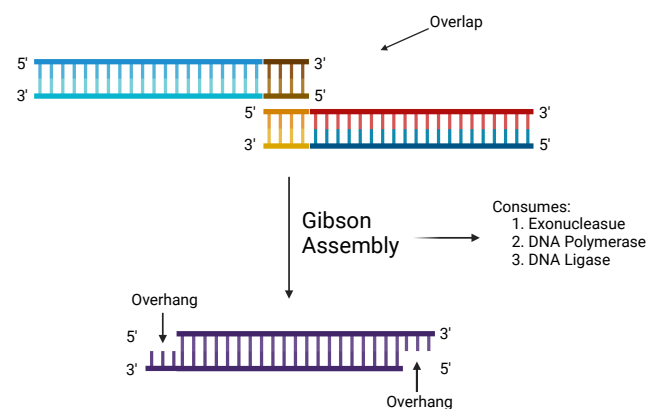


Fig. 4 This image illustrates a top level view of the Gibson assembly protocol. It begins with two separate overlapping DNA strands and ends with a single combined strand with two overhangs. This figure was created with Biorender.com.

^{**} **Electrowetting** refers to the ability of an applied voltage to modulate the “wettability” of a surface⁴¹

3 DNA Assembly and Droplet Routing

3.1 Automated DNA Assembly

There are two requirements a DNA oligo library must have for successful DNA assembly.

1. DNA oligos must be assembled to represent arbitrary data
2. DNA oligos can be joined simultaneously in one Gibson assembly process without risking mis-alignment.

The first requirement implies oligos can be assembled in any permutation. The second requirement assumes a specific order to the oligos to allow simultaneous assembly. These two conclusions are contradictory. To ensure desired ordering, it is necessary for segments to be uniquely matched with one another.

We resolve this contraction with a dual library of oligos we call "symbols" and "linkers" illustrated in Fig. 6. These "symbols" allow us to represent arbitrary data when assembling them together. These "linkers" allow massive parallelization between symbol assembly and ensure correct ordering. This dual library covers the first and second requirements.

Data genes will comprise long chains of alternating symbols and linkers, with relevant information contained in the symbols. All symbols will have unique interior segments composed of 8 base pairs, allowing each to encode 16 bits. By using multi-bit symbols instead of assembling one base pair at a time, we exchange much of the fabrication time for overhead in maintaining the symbol library. All symbols share the same beginning (*left-side*) and end (*right-side*) sequences, but these two sequences are different from each other. The left and right ends will not be complementary, disallowing direct Gibson assembly of two symbols. Complementary ends will be shared by all linkers, but each linker will only have one end matched with those of the symbols. The other end will bind with its unique, complementary linker. Thus, any desired chain of symbols can be assembled by first using Gibson assembly to separately attach each symbol to the appropriate linkers and then bringing all attached symbol-linker pairs together in another Gibson assembly process. The linkers will naturally order themselves according to their unique matches and the symbols will automatically fall into the appropriate order. This process is demonstrated in Fig. 5. Following assembly, the new string of symbols will undergo purification and polymerase chain reaction (*PCR*) multiplication of the correctly assembled product. This product is a storage gene which holds encoded information (in its symbols) and non-coding connective DNA (in its linkers).

Any gene requiring more symbols than what can be reliably handled by a single assembly process can be constructed by numerous sequential assembly processes. Each process will consist of a safe manageable number of individual segments, themselves composed of one or more symbols and associated linkers. This will allow reliable fabrication of arbitrary sequences of symbols using the same library. Readout can be assisted by a bookend sequence shared by every linker that marks the space between each symbol. This process does not require macroscopic chemical reagent droplets, and can in theory be miniaturized to the domain of microscopic droplets found on a DMFB.

Assembling extremely large data sets comprising of billions of symbols will require vast numbers of individual Gibson assembly operations. This presents a non-trivial problem in the form of managing droplet traffic routes and congestion. Given an arbitrary list of symbols to be encoded in a gene, droplets must be created, destinations chosen, and routes carefully controlled. This multi-step process necessitates an automated system capable not only of routing traffic but also deciding what Gibson assembly operations must be performed and when to build the desired gene.

3.2 Routing Algorithm for Droplet Pathing

Our system routes droplet traffic to desired Gibson, PCR, and purification sites using prioritized 3-D A* on the DMFB. First, generic A* will be explained, and then prioritized 3-D A* applied in our practice will be introduced.

The goal of A* is to find the lowest cost path from point A to point B on a given graph. A graph is a generic collection of nodes connected via edges, and cost refers to the length of the path. The cost for paths are calculated using two scores, referred to as g and h scores. The g score is the cost to get to the current node (the path already traversed), and the h score is the distance from the current node to the end node (the path to traverse). This h score is determined via a specific user-chosen heuristic; however, our implementation of A* uses Manhattan distance. The h and g scores are added to become the f score, or the total score for the path. Fig. 7 details an example of A* on two droplets moving in 2-D space. Ideally, the f score should be as small as possible⁴⁹.

Starting from point A, we look at each edge extending out from A and calculate the f score for the surrounding nodes. The nodes and f score is placed into an open set, usually represented as a data structure in memory. From there, paths are extended by looking at each node in the open set, starting with the lowest f score. The f scores for the nodes connected to the current node are then updated and placed back into the open set. This continues until B is reached or it is concluded no path to B is available.

To contextualize this algorithm, the nodes in the graph represent grid spaces on the DMFB, and edges indicate which grid spaces are next to each other. In the explanation below, point A represents a droplet's starting position while point B is its local destination which can be one of many things. It can be an intermediate location where the symbol and linker droplets mix into a larger droplet. It can also be a location where Gibson mixing occurs between the larger droplet and a Gibson mix reagent droplet. For both situations, this goal location is the site of droplet mixing in some form. We classify the collection of these droplets as a merge group.

We adapt generic A* in our application to prioritized 3-D A*. It is prioritized because the algorithm prioritizes routing the droplet with the furthest Manhattan distance to travel first. It operates on 3 dimensions with two dimensions representing the DMFB 2-D grid layout and the third representing time. All droplets are routed sequentially using the 3-D A* priority scheme. All droplets must move one grid space at a time simultaneously as all routes are planned beforehand. The algorithm is called N_D times, where

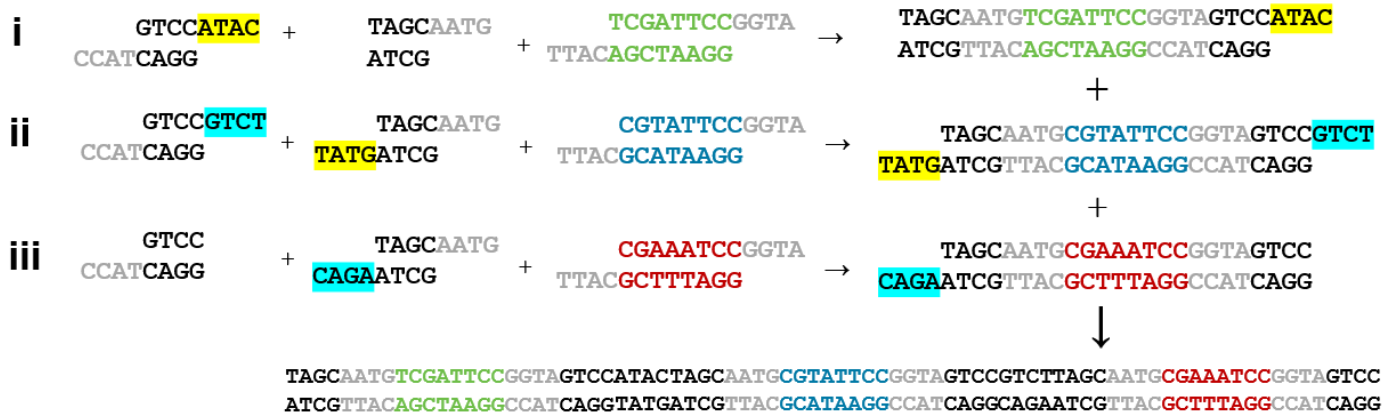


Fig. 5 A graphical representation of the symbol-linker assembly process. A set (i-iii) of three symbols are joined to two linkers each in a first reaction. The resulting one-symbol assemblies are assembled in a second reaction into a three-symbol assembly via the linkers.

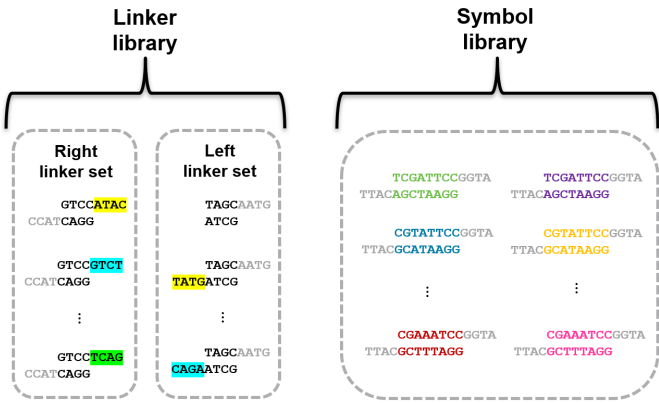


Fig. 6 An example of a linker library and a symbol library. The Linker library contains two sets of linkers: a Right Linker Set that attaches to the right end of a symbol, and a Left Linker Set that attaches to the left end of a symbol. Universal overhangs (in gray) are used to attach any linker to any symbol. The highlighted regions of the linker sets are complementary to each other, so that they can link together specifically during a Gibson reaction.

N_D is the number of droplets on the grid. 3-D A* would be called once per newly pulled droplet. Once each droplet has its route, they will move together one time step at a time. The A* algorithm itself is called upon every merge operation and route completion as the resultant droplet now needs to be assigned a new route. A visualization of such routing movement is shown below in Fig. 8

To prevent unwanted merging of droplets, the notion of a droplet shadow and occlusion zone are introduced, which are visualized in Fig. 11. These are projected into a 3-D space such that for N_D droplets, there are $3N_D$ occlusion zones where each occlusion zone is present for the previous, current, and future time step of the droplet. Droplets which are not in the merge group of the current droplet see the occlusion zones as obstacles they must route their path around. Since routing is completed by taking all 3 dimensions into consideration and before any droplet movement occurs, the obstacles are static meaning they do not appear at random to block a droplet's route. This method of routing is advantageous because it prevents unwanted collisions from occurring while having each droplet take the optimal path given

Time Step	G Score (Red)	H Score (Red)	G Score (Blue)	H score (Blue)
0	0	6	0	5
1	1	5	1	4
2	2	4	2	3
3	3	3	3	2
4	4	2	4	1
5	5	1	5	0
6	6	0	5	0

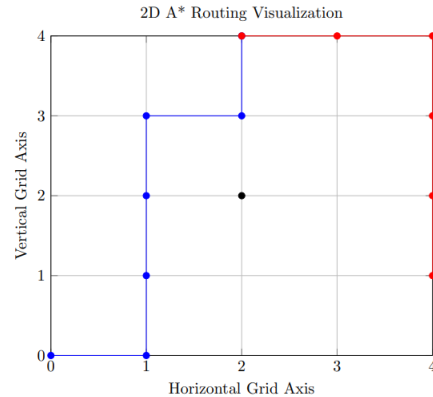


Fig. 7 The top table shows the F and G scores for each path at every time step. The bottom figure illustrates 2-D A* with a simple example for 2 droplets shown in a 2-D plane. These 2 droplets wish to mix at the goal coordinate (2,4). The droplet corresponding to the blue route starts at (0,0), the droplet corresponding to the red route starts at (4,1). Both droplets must consider an obstacle located at (2,2) while computing route calculations. The blue route will be calculated first due to the fact that it has the largest distance to the goal coordinate. The red route will then be calculated after. The table contains both the G and H scores of each path at each time step for the taken paths.

the constraints imposed by previously routed droplets.

Section 4 depicts an end-to-end software system using a virtual lab to simulate movement on a physical DMFB. It addresses the routing problem using the aforementioned 3-D prioritized A* algorithm to route droplet traffic. Together, it presents a solution to the task of automatic gene assembly through droplet routing and mixing.

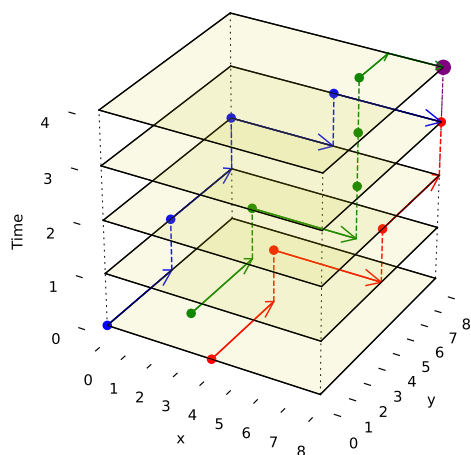


Fig. 8 This figure illustrates 3-D routes with a simple example for 3 droplets. These 3 droplets wish to mix at the goal coordinate (8,8). The droplet corresponding to the blue route starts at (0,0,0), the droplet corresponding to the red route starts at (4,0,0) and the green droplet starts at (2,2,0). Every movement of the droplet is shown by increasing the time value (z-axis value) by 1. The A* algorithm is projected to the 3-D space, and the blue route is planned first because it has the farthest Manhattan distance to travel. The routes are designed to avoid unwanted collision with each other until they reach the desired location as no paths intersect. The merged droplet, which is bigger, is shown in purple at (8,8,4).

4 Architecture

We use a modular hierarchy to solve the droplet traffic management problem, shown in Fig. 9. At the top of the hierarchy we have the compiler, which is responsible for reading the user's desired product P and making a breakdown of the basic chemical steps that must be performed to create it. These basic chemical codes are passed down to the manager, which is responsible for assigning the droplets' destinations and giving commands to the virtual lab. The manager is analogous to a human operator who is given a set of chemical reactions to perform and manually controls droplet movements to execute them. At the bottom of the hierarchy is the virtual lab, which emulates a real DMFB. The lab houses a group of electrowetting gridspace and chemical droplet objects, which represent their physical equivalents and behave in similar ways within their virtual space. These three modules communicate downstream using structured codes.

Such a modular architecture makes it easy to modify specific elements of the hierarchical structure described above. The compiler can be modified to consult a different protocol without affecting the manager's operation. Likewise, the manager's routing algorithm can be changed without affecting the lab's execution of the commands it is given. The lab's droplet dynamics model can also be modified and improved independently. It is only necessary that the instruction and chip command codes used to send messages downstream remain unaltered.

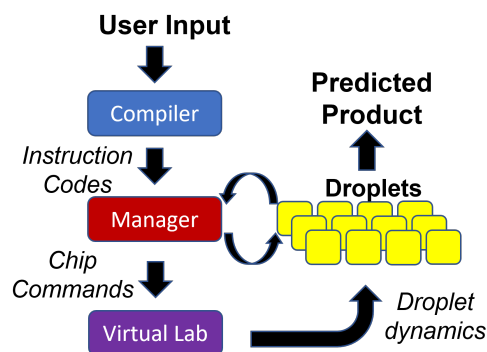


Fig. 9 Block diagram of the software modules that plan and execute the automated gene assembly. The Compiler reads the desired input and consults a preprogrammed chemical protocol to generate the necessary chemical operations and properly order them. The Manager reads the resulting instruction codes and coordinates the creation, destination selection, and routing of droplets. The virtual lab provides feedback on droplet movements to the manager.

4.1 Assembly Protocol

To automate construction of user-determined strings of DNA, the system will require an assembly protocol to follow. We define this protocol to fulfill the following conditions.

1. The protocol must take multiple independent pieces of double-stranded DNA and attach them to one another in the designated order.
2. The protocol must consist of a simple set of operations such as mixing and moving.
3. The protocol must always consist of exactly the same operations for a given number of strands.
4. The protocol must be applicable to its own products; that is, it should be recursive.

An instruction produced by the protocol always takes the form of a list in the following format: [\langle InstructionType \rangle , \langle droplet1 \rangle , \langle droplet2 \rangle , ...], where \langle InstructionType \rangle is a string. The reagent \langle droplet1 \rangle is a list of strings itself where [\langle reagent1 \rangle , \langle reagent2 \rangle , ... \langle reagentN \rangle] represents a single droplet containing N reagents although it is often the case that $N = 1$.

When reading the instructions, the manager will execute a case structure based on \langle InstructionType \rangle using component droplets matching the descriptions given by \langle droplet1 \rangle , \langle droplet2 \rangle , etc. An example instruction might be ['GibsonMove', [$_S0_$], [L1], ['gibson-mix']], indicating that the manager should identify three droplets containing the symbol 0, the linker 1, and some Gibson mix and bring them together on a suitable Gibson site.

An example of the instruction codes for a single assembly step using the Gibson symbol-linker protocol is given below. This list assembles the data string S1-S0-S2.

1. ['Gibson-Move', ['L0'], [$_S1_$], ['gibson-mix']]
2. ['Gibson', ['L0', $_S1_$], 'gibson-mix']
3. ['Gibson-Move', ['L1'], ['L2'], [$_S0_$], ['gibson-mix']]
4. ['Gibson', ['L1', 'L2', $_S0_$], 'gibson-mix']

5. ['Gibson-Move', ['L3'], ['_S2_'], ['gibson-mix']]
6. ['Gibson', ['L3', '_S2_'], ['gibson-mix']]
7. ['Gibson-Move', ['L1_S0_L2'], ['L3_S2_'], ['_S1_L0'], ['gibson-mix']]
8. ['Gibson', ['L1_S0_L2', 'L3_S2_', '_S1_L0'], ['gibson-mix']]
9. ['Purify-Move', ['_S1_L0L1_S0_L2L3_S2_'], ['purify-mix']]
10. ['Purify', ['_S1_L0L1_S0_L2L3_S2_'], ['purify-mix']]
11. ['PCR-Move', ['_S1_L0L1_S0_L2L3_S2_'], ['PCR-mix']]
12. ['PCR', ['_S1_L0L1_S0_L2L3_S2_'], ['PCR-mix']]

In the list above, the first two steps create the symbol-linker droplet ['_SI_L0'] through Gibson moving and mixing steps. The first instruction has instruction type 'Gibson-Move' with three droplets containing the linker 0, the symbol 1, and some Gibson Mix. It will move the droplets to an available Gibson site. The second step initiates Gibson mixing and assembly on the three droplets to form the chain ['_SI_L0']. Likewise, steps 3 to 6 produce the droplets ['L1_S0_L2'] and ['L3_S2_']. Steps 7 and 8 take these three larger droplets and perform Gibson assembly on them at a suitable Gibson site. This creates the droplet ['_S1_L0L1_S0_L2L3_S2_']. The final four steps take the final droplet to purify (clean) and to PCR (amplify) sites to create the final data string S1-S0-S2 held together with linkers.

4.2 Compiler

Among the components of the architecture, the compiler is closest to the user, which means it is also the most abstracted, having no knowledge of the actual droplets and movements which take place under the hood. The compiler is not connected to the lab where all physical processes occur. It is analogous to a code compiler which translates a user input into a set of primitive instructions. Here, the compiler input consists of a list of characters representing the aforementioned "symbols" such as 'S1-S0-S2'. The compiler must determine how to build the given DNA strand by repeated and recursive applications of its assembly protocol. We designate the desired final product P , with a length of L_P symbols.

The compiler must first determine how to construct P using assembly operations that can combine at most N_A segments at a time, with the limit N_A being set by the assembly protocol. In this case N_A is the reliability margin of the symbol-linker Gibson assembly. We employ a N_A -ary data tree to store the construction blueprint. The root node stores P . The compiler symbolically breaks P up into N_A separate segments and stores each segment in a child node below the root. These segments themselves are broken up in the same way, with new nodes storing the new, smaller segments. The tree is built from the bottom up until the final nodes contain segments of one symbol in length. This abstract string-building will be mimicked by the DNA strand assembly. Algorithm #1 and Algorithm #2 explain the algorithms for building the assembly tree step-by-step. We note that some of the algorithms in this manuscript do not lend themselves well to formal pseudocode with high readability, prompting the decision to use informal verbal descriptions for all processes instead. Thus, while the steps are easy to understand, not all details are included.

With the ordering of the tree determined, the compiler can then fill in the instructions for each node by consulting the protocol

Algorithm 1 Data Partitioning (Inputs: data list, N_A)

1. If data length (L_P) does not exceed N_A , break data into singlets and return.
 2. Otherwise, break data into L_P/N_A N_A -tuplets.
 3. Add a final, shortened tuple for any data remainder.
 4. Return list of tuplets.
-

Algorithm 2 Build Assembly Tree (Inputs: gene list, N_A)

1. Create a list of nodes, one for each symbol in gene.
 2. While node list length exceeds N_A , repeat 3–8.
 3. Partition the node list using Algorithm #1.
 4. Empty the node list.
 5. For each sublist in node partition, repeat 6–8.
 6. Create a parent node above all nodes in sublist.
 7. Create instruction list for parent node using Process #3.
 8. Append parent node to nodelist.
 9. Once node list is less than N_A nodes long, create root node above all nodes remaining in list.
 10. Create instruction list for root node using Algorithm #3, then return.
-

and giving the strands of a node's children as its inputs. This is outlined in Algorithm #3. This implies nodes without children (leaf nodes) have no instructions. The resulting 'assembly tree' provides a blueprint for constructing the final product P . The leaf nodes, each holding one symbol, can be read from left to right to give the individual symbols of P . The first layer of non-leaf contain the N_A -length products of the first set of assembly operations as well as the instructions needed to carry them out. The next layer further groups those segments in length N_A^2 , and so on. The root node contains instructions for the final assembly of P , grouping the remaining segments together. See Fig. 10 which depicts the assembly tree data structure used to assemble 'S1_S0_S2_S4' with linkers omitted. The instruction codes for assembling 'S1-S0-S2', described above in the Assembly Protocol subsection, are carried by the left-hand instruction node in the graphic.

Algorithm 3 Generate Instructions (Inputs: node, linker-list)

1. Create list of subgenes in node's children.
 2. For each subgene, repeat 3–6.
 3. Select 3' and 5' linkers, if any.
 4. Create empty instruction list.
 5. Add 'Gibson-Move' command to instruction list with non-mixed subgene and linkers as variable reagents.
 6. Add 'Gibson' command to instruction list with mixed subgene and linkers as variable reagent.
 7. Add 'Gibson-Move' command to instruction list with non-mixed subgene-linker sets as variable reagents.
 8. Add 'Gibson' command to instruction list with mixed subgene-linker set as variable reagent, then return.
-

Besides encoding the organization of substrings and the individual instructions necessary to chemically assemble P , the nodes also interface with the manager in real-time to track the disposition of droplets created for each node. This will be discussed in more detail below.

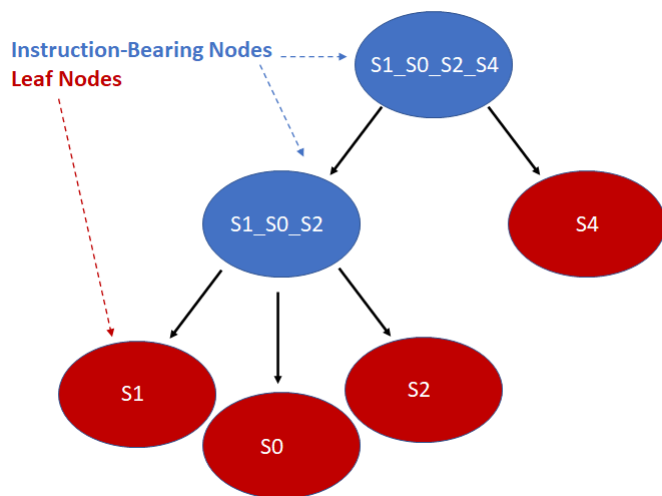


Fig. 10 Simplified diagram of a small assembly tree data structure. In red, the leaf nodes each contain a single symbol. The root node represents the final desired symbol sequence, or gene. Non-leaf nodes contain assembly instructions readable by the Manager. We note that the linkers between the symbols have been excluded for readability. See Fig. 13 for more details on individual nodes.

4.3 Lab

The lab was created to handle the problem of droplet simulation. In order to manage droplets, the droplets must have somewhere to live. In the absence of a physical DMFB chip and appropriate sensors to track droplets in real-time, we create a virtual DMFB, independent of the manager, and interact with it by feeding it commands just as with a real DMFB. This virtual lab is able to inform the manager when its commands result in mistakes such as the accidental mixing of droplets intended for separate destinations. This allows rapid testing of the manager and compiler and their various subroutines, such as routing and destination assignment. A simulation bed greatly accelerates development for an automated system prior to deployment on actual devices.

The lab simulates each droplet and each DMF gridspace as independent objects in a continuous loop representing the passage of real time. At each time-step the lab checks for any update commands, activating or deactivating the corresponding gridspace if any. Then each droplet checks its surroundings for active gridspace and updates its location according to the droplet movement model. For convenience, all droplet objects maintain references to each gridspace they currently contact, and each gridspace object similarly holds references to any and all droplets touching it. This location update step is where the lab detects errors.

The droplets track their current ‘shadow’, which is a digitization of the droplet’s shape. Assuming a droplet is centered in the middle of a gridspace, the shadow is a list of gridspace coordinates, relative to the center space, which also touch the droplet. This is used by the manager to determine which electrodes to use for moving the droplet. This also allows easy calculation of an occlusion zone, the layer of gridspace around a droplet that are as close as possible without touching. This layer is used as a barrier, off-limits to all other droplets that are not intended to mix. For instance, a small droplet that only touches the gridspace nearest

to its center in the four cardinal directions would have a shadow $S = [[0,0], [1,0], [0,1], [-1,0], [0,-1]]$ and an occlusion zone $O = [[1,1], [1,-1], [2,0], [0,2], [-1,1], [-2,0], [-1,-1], [0, -2]]$ as shown in Fig. 11. As droplets merge and grow, their shadows and occlusion zones increase commensurately. During routing, a droplet’s shadow and occlusion zone is projected both forward and backward in time by one step to ensure no undesired mixing can happen.

Like the compiler instructions, the commands for controlling the lab use a simple structured language to facilitate automatic interpretation. There are many possible actions that can be taken at numerous points around the lab. Only a small fraction of the available actions are taken in any one round. Therefore, we use a hash map to pass the commands, with keys being `<CommandType>` and associated values being a list of grid-point coordinates at which `<CommandType>` should be executed. Some commands require additional data and thus the keys may come in pairs such as ‘ActivateIndices’ and ‘ActivatePotentials’, the first key holding a list of gridpoint coordinates to activate and the second key giving the respective electrostatic potentials for each gridpoint. The hash map command layout allows the manager to construct many similar commands throughout its loop and simply append them to the appropriate key’s stored value. The lab, on its turn, will simply check each extant key and execute the relevant operation at each given location.

4.4 Manager

With a simulated lab to house the droplets and a compiler to provide the basic mix and merge instructions, there is one final task. The instructions must be translated into actual commands for the lab to execute. This entails selecting reservoirs from which to pull droplets of appropriate types, choosing destinations for them and determining routes that will see them to their destinations without any unwanted misadventures along the way. This is the manager’s job. The manager interfaces with the assembly tree and the lab. It runs in a loop matching the lab’s time-steps, providing new commands at each step while also tracking long-term progress towards each assembly node’s instructions.

The manager must be able to track the droplets in the lab, knowing their locations and contents at each step. It is useful to reference droplets by their contents rather than location, since this allows easy matching of droplets to instructions which call for specific reagents. However, there is a duplicate problem. The reagents used in any given assembly are likely to be used by many other parallel assemblies. If droplets were referenced by contents, it would be difficult to distinguish between identical droplets intended for two separate assemblies. Therefore, rather than storing all droplet references in one structure, each node is given a hash map which links it to specific droplets. A node’s droplets are those created in direct response to its instructions in addition to those inherited from that node’s children.

Thus although each droplet may not be unique on the lab, it is unique within its node’s hash. Identical droplets intended for different destinations are easily distinguishable. Droplet hash keys are similar to the reagent references in the assembly instruc-

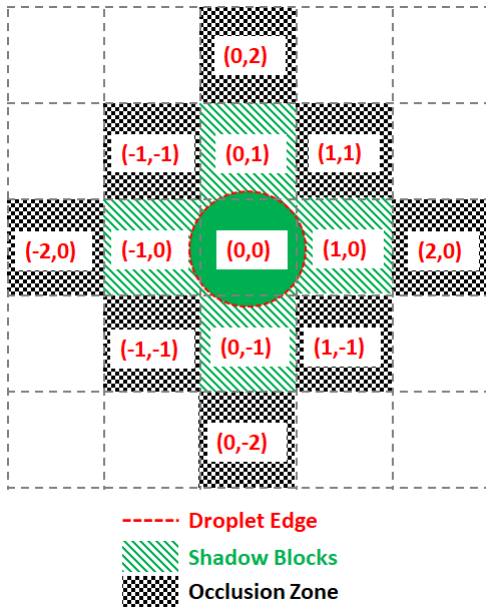


Fig. 11 Diagram of the digitization of droplet shadow and occlusion zones. A droplet centered on a gridspace with relative coordinates (0,0) has a sufficient radius to touch the four nearest neighboring gridspace, making five shadow blocks. All gridspace adjacent to the shadow blocks are designated as occlusion zones.

tions. The keys are the alphabetically sorted tuple of free-floating species contained within a droplet, with one entry per species. For example, a droplet containing Gibson mix, symbol 0 and linker 1 would be matched by the key ('L1', '_S0_', 'gibson-mix'). However, after the droplet undergoes the Gibson process—consuming the Gibson mix along the way—and the symbol-linker pair are combined to form a single DNA species, the key changes to reflect the new state: ('_S0_L1'). See Fig. 12. Note that after Gibson assembly the ordering of the symbol and linker in the key have changed. The symbol and linker keys represent actual double-stranded DNA which link together in a preferred direction, and the new key reflects this, rather than presenting them in alphabetically sorted order as was the case for free-floating species prior to combination.

We now have a complete description of the information contained in the Node objects. As shown in Fig. 13, they contain immutable *data* and *instruction* values consisting of the symbol-linker representation of the DNA strand they construct and the instructions used to build it. They also contain a mutable dictionary of droplet objects as discussed above, which changes throughout the manager-lab time loop.

The manager runs in a loop lock-stepped with the lab, maintaining a list of active nodes drawn from the assembly tree and stepping through their instructions in parallel. It also creates a list of lab commands which begins each iteration empty, fills up during the node advance and droplet routing steps, and is subsequently passed to the lab for execution. For each iteration, it runs four processes in order as shown in algorithm Initially, the active nodes list consists of all of the lowest-level non-leaf nodes.

When checking node progress, the system evaluates the node's

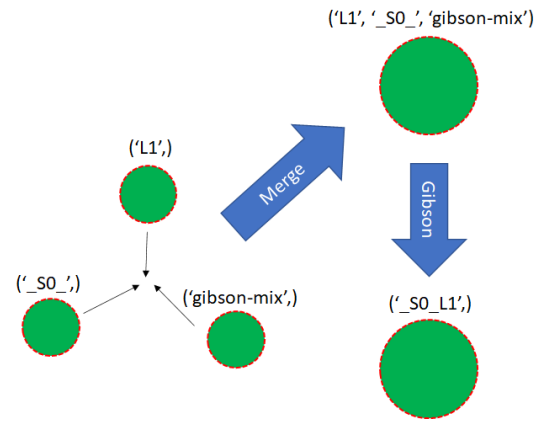


Fig. 12 Three single-species droplets merge, becoming a larger droplet with mixed species. The droplet undergoes Gibson assembly, becoming a different species. The droplet keys used by the Manager are shown for each.

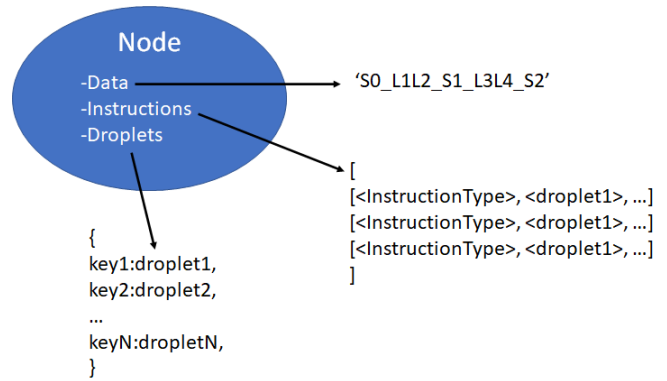


Fig. 13 Detailed contents of an assembly tree node object. Three items are carried by each non-leaf node. The data string, corresponding to the sequence of symbols and linkers produced by the node. Instructions, a list of the requisite fluidic and chemical operations. Droplets, a mutable hash map of currently extant droplets being used for instructions by this node on the virtual lab.

current instruction list and its droplet's location and see if the node is ready to move to the next instruction. If the node is ready to advance its instructions, it will check the instruction codes and advance to the next instruction.

After finishing with the nodes, the manager checks for droplets that have either been newly assigned to destinations or were unable to route last iteration. The manager attempts to plan a route for each of these.

The manager's routing algorithm uses a prioritized A* method. Droplets are organized into 'merge groups', which are collections of droplets that are seeking to combine into one conglomerate. All routes that are generated obey the following anti-collision constraint that applies to any two droplets d_x and d_y of different merge groups. Any gridspace occluded by d_x until time t_a may not be overshadowed by d_y during any time t_b such that $(t_a - t_b) \geq 0$. With priority given to merge groups containing droplets with the farthest Manhattan distance to travel, all selected droplets are routed one at a time using a 3-D A* graph traversal. Two of the dimensions represent the virtual—or physical—DMFB grid lay-

Algorithm 4 Complete one Timestep Iteration (Inputs: node)

1. Check Node Progress.
 2. Advance Node Instructions.
 3. Plan Routes for Unrouted Droplets.
 4. Execute One Round of Commands.
-

out, while the third is time. For each droplet d the router takes droplet shadow S_d and occlusion zone O_d into account at every step, projecting them into the 3-D space. These zones are off-limits for other droplets during their own routing phase. This includes droplets that will be routed during this or any future time-steps. The space is initially free of occlusion zones when the highest-priority droplets are routing and becomes more populated as the other droplet routes are filled in. Of course, there may also be occlusion zones generated by the routing phase in the previous time-step, which all droplets during this time-step must avoid regardless of their priority level. There will be at most $3N_D$ occlusion zones present on the grid at a given time, where N_D is the total number of extant droplets. This is because each droplet generates occlusion zones for its most recent, current, and immediately subsequent steps to satisfy the anti-collision constraint. This routing method allows many droplets to move simultaneously while avoiding unwanted collisions. Furthermore, each individual droplet takes the optimal path within the constraints given to it by the droplets higher in the priority queue and the droplets routed during previous time-steps.

We note that the modularity of the system makes it relatively easy to implement a different routing scheme. Incorporating more advanced electrowetting technology which allows for more flexible movement and improving the routing algorithm to be more efficient would only require the redesign of the routing subroutine itself, leaving the other parts of the software to function as normal. Possible redesigns may include a contamination aware⁵⁰ routing algorithm already designed in 2009 or incorporating Moving Target D* Lite⁵¹ which has been shown to be effective in problems where obstacle occurrences appear dynamically over time. Extensive literature exists regarding routing algorithms on DMFBs which may be considered in future iterations to improve routing algorithm runtime and complexity as surveyed in Section 1.4.

After planning routes for all droplets, the manager will perform the movement of droplets according to the instructions and routes set up by the first three droplets. After these steps complete, one loop iteration is concluded.

5 Results and Discussion

5.1 Simulation Results

Having presented the architecture for our automated DNA assembly system, we present simulation results regarding the performance of our software system on a virtual lab. Our simulation does not incorporate physical latencies present with physical DMFBs such as electrode switching-rate⁵² and mixing operations⁵³. For this reason, we note the reader should not compare the runtimes found in our simulation to existing DNA synthesis technology as these runtime results are meant to capture trends

in system performance over various intentional modifications.

In our simulation, we wish to evaluate the impact of computer hardware, virtual lab grid size, and target gene length on our system's performance. We draw conclusions of their impacts from the system's runtime, memory usage, and CPU usage. The simulated DMFB system for DNA assembly was written in Python3. Fig. 14 displays a snapshot of the simulation's GUI displaying routed droplet movement in real time. Additionally, benchmarking results were captured to better understand the distribution of function workload and the limitations of the current model.

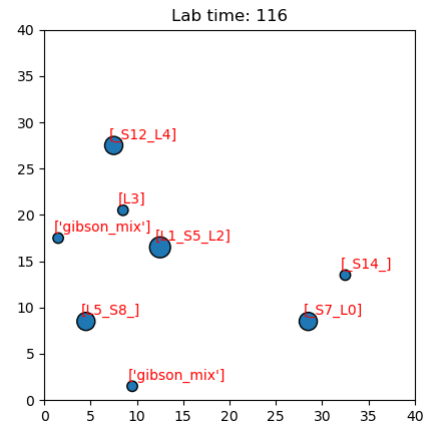


Fig. 14 Image of the simulation's GUI displaying droplets being routed in a 40×40 size grid. The number of full command execution rounds are shown at the top as the lab time.

5.1.1 Hardware Results

The program was executed on three different machines with varying CPU and random access memory (RAM) capabilities at a constant grid size of 1000×1000 gridpoints (see Table 3 for machine specifications). Table 3 displays the simulation's runtimes in correspondence to hardware specifications. The amount of RAM the simulation consumes is not limited by the available RAM of any of the used machines as all three machines had sufficient RAM to run the simulation. It is therefore unlikely that RAM availability will be a critical component in reducing runtime.

The data gathered in Table 2 shows that peak RAM usage is approximately constant, about 1.3Gib, across all machines when run on a grid size of 1000×1000 gridpoints. This is not an unreasonable amount of RAM consumption as the simulation will not consume a tremendous amount of a user's available RAM.

However, the simulation consumes an entire CPU thread on each of the three machines. It is likely CPU usage is constraining the system from running faster as it immediately uses the entirety of a thread, making it a limiting factor in system performance. We analyzed the CPU efficacy using a metric called "thread rating," which is a metric that represents performance of a single CPU core. As the thread rating increases, the runtime decreases. The relationship between thread rating and runtime is decreasing and exponential. Increases in thread rating for lower end consumer machines leads to a large decrease in runtime whereas upgrading the thread rating for a higher end machine sees diminishing

Table 2 RAM statistics vs. System Hardware. The RAM Usage was approximately the same across the three machines when run on a grid size of 1000×1000 gridpoints. There are variations in total RAM, but all machines have enough RAM to support the memory required to run the simulation. Machine 3 had the fastest RAM data rate of 3200 Mega Transfers per second (MT/s), the other two machines had RAM data rates of 2400 MT/s.

Machine	Peak RAM Used	Total RAM	RAM Speed
1	1.4GiB	16GiB	2400MT/s
2	1.3GiB	32GiB	2400MT/s
3	1.2GiB	32GiB	3200MT/s

returns on decreasing runtime.

Table 3 Simulation Runtime vs. System CPU Hardware. Thread rating is a metric obtained from PassMark Software's extensive database of CPU benchmarks and tests. The thread rating indicates the performance of a single logical CPU core. The units for the thread rating are *MOps/Sec*⁵⁴.

Machine	Thread Count	Thread Rating	Runtime (s)
1	8	1903	7234.69
2	8	2417	3191.83
3	16	3143	1962.33

The CPU usage results are also summarized in Table 3. The simulation completely consumes one CPU thread on each machine. Since Machines 1 and 2 have 8-thread CPUs, they yielded around 12.5% CPU usage. Meanwhile, Machine 3 has a 16-thread CPU yielding around 6.25% CPU usage.

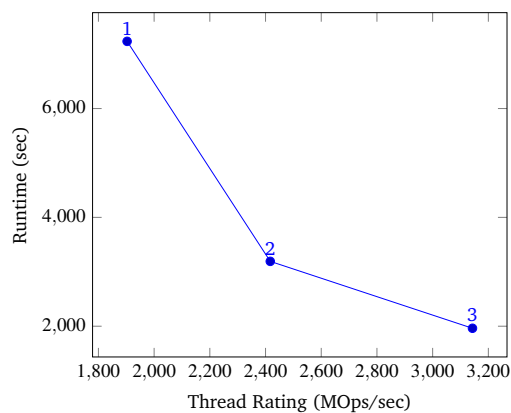


Fig. 15 Simulation Runtime vs. Thread Rating. Data points are labeled by the corresponding machine number, see 3. As the thread rating increases, the runtime decreases. Intuitively there's a diminishing return on decreasing runtime with an increase of thread rating. A non-asymptotic relationship between thread rating and runtime would imply computations could be done instantaneously with substantial thread ratings.

5.1.2 Grid Size Results

The program's performance was evaluated across a range of grid sizes on a single machine. Here, we used Machine 3. With respect to grid size, runtime responded exponentially (Fig. 16), memory usage responded linearly (Fig. 17), and CPU usage responded constantly (Fig. 18). For very large grid sizes, RAM

availability will become the limiting factor to affect runtime as a linear increase in grid size yields a linear increase in Peak RAM usage. Once Peak RAM usage becomes nears the maximum available RAM, performance will deteriorate substantially. The CPU metrics do not have much impact on the runtime when sweeping across large grid sizes as they continue to consume the entirety of one thread.

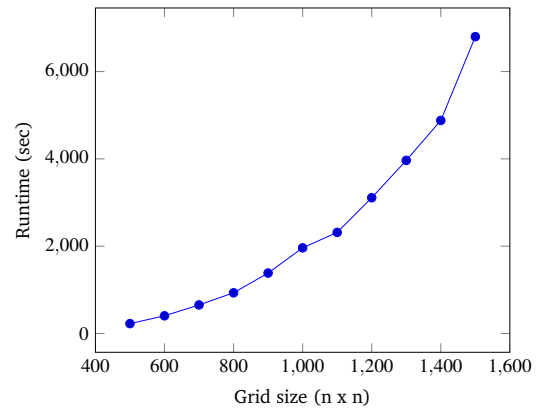


Fig. 16 Runtime vs. Grid size ($n \times n$). The runtime of the simulation synthesizing a gene of length 5 was captured for grid axes lengths of 500 to 1500. There is a clear exponential increase in time with linear increase in grid size.

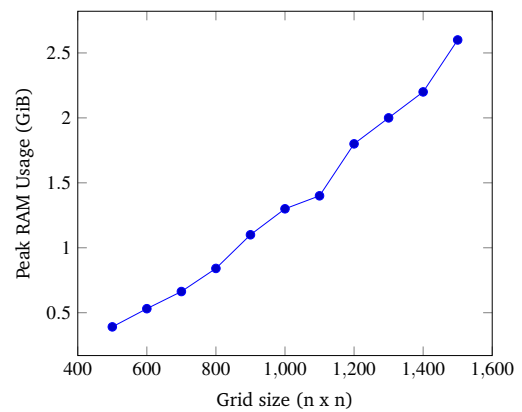


Fig. 17 Peak RAM Usage vs. Grid size ($n \times n$). The peak RAM usage (in GiB) of the simulation synthesizing a gene of length 5 was captured for grid axes lengths of 500 to 1500. There is a clear linear increase in memory consumption with linear increase in grid size.

5.2 High Impact Functions

The open-source visualization software Gephi was used to record the runtimes of the simulations local functions over three trials. The trials were chosen such that as the problem size increased, the congestion remained constant. In the context of these trials only, congestion is computed as the total number of droplets pulled from reservoirs divided by the number of total gridpoints. The exact simulation input parameters are displayed in table 4.

In these trials, the functions `Advance` and `Route_Droplets` were identified as methods of interest. The lab's function `Advance`

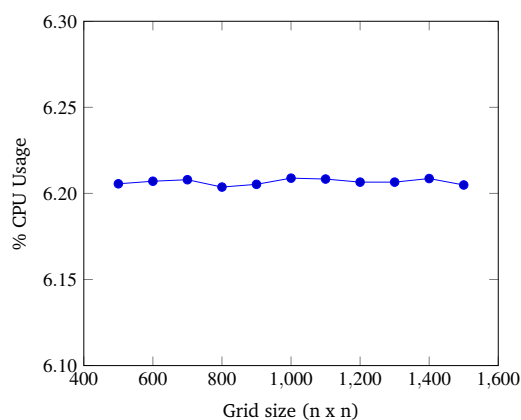


Fig. 18 Average CPU Usage vs. Grid size. The Average CPU usage of the simulation synthesizing a gene of length 5 was captured for grid axes lengths of 500 to 1500. For all grid sizes, an average of 99% of a single thread was consumed. Because the machine has 16 threads, the results showed slightly less than 6.25% of CPU used across all grid sizes. There is no meaningful impact on CPU usage from changed grid sizes.

Table 4 Local runtime trials. The table illustrates the rationale behind the parameters used in each trial displayed in Fig. 19. The parameters for these trials were chosen such that the local runtimes of the simulation’s functions could be examined as the problem size increases but the congestion remains constant. In this situation congestion is measured as the ratio of the total number of droplets pulled from reservoirs to the number of gridpoints. Droplet counts and grid sizes are discrete, thus the congestion is only approximately constant.

Trial	Grid Size	Gene Length	Droplets	Congestion
1	50	2	9	0.00360
2	76	4	21	0.00364
3	96	6	33	0.00358

computes an entire time step of the simulation. `Advance` iterates over the gridpoints and droplets multiple times in order to update their contents. The manager’s function `Route_Droplets` computes the routes for droplets that have yet to be routed with the prioritized 3-D A* routing algorithm. The proportion of the total runtime spent computing each function is shown in Fig. 19. As the problem size increases, `Advance`’s proportion of runtime increases. The proportion of the time consumed by `Route_Droplets` also increases as the problem size increases, overtaking the combined runtime of all other subroutines. In the last trial it is evident that these two functions will dominate the share of the simulation’s runtime as larger, more realistic input parameters are chosen. It may be inferred that the computation of `Advance` on an exponentially increasing input tends to be slower than the computation of the prioritized 3-D A* routing algorithm on a linearly increasing number of pulled droplets.

Improving the runtime of `Advance` is worth attention in future development. This task is difficult as it requires an optimized approach to iterating over all gridpoints and droplets. Additionally, this is a function that runs on the simulated lab, and it is likely the speed of advancing droplets on a real DMFB will be different. The simulation may benefit in runtime by considering alternatives to the prioritized 3-D A* routing algorithm used in `Route_Droplets`.

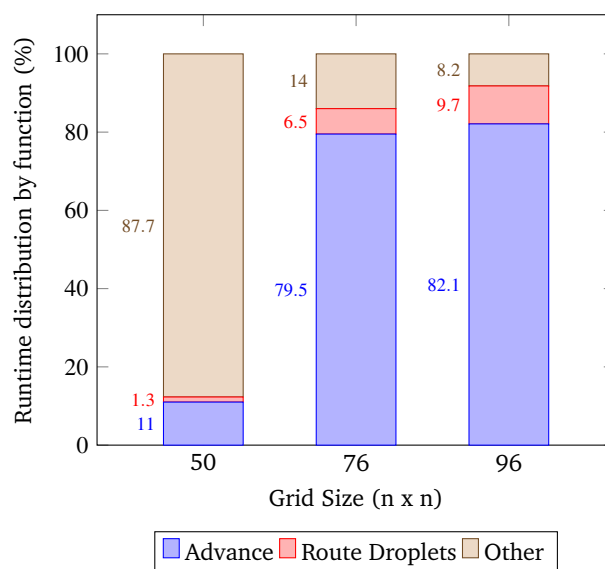


Fig. 19 Runtime distribution by major function. This data was obtained by running the simulation at an approximately constant congestion ratio. Where this congestion ratio is the total number of droplets pulled from reservoirs divided by the number of gridpoints. The approximate constant congestion ratio used was 0.0036 droplets/ $gridsize^2$ which was chosen out of convenience. The parameters for these trials are shown in 4.

Currently, the algorithm considers all possible routes for each droplet; however, there may be room for improvement by implementing methods that return an acceptable suboptimal route while only evaluating a fraction of the input space. Finding an acceptable suboptimal route for problems which can face a lot of congestion and time consumption has been studied by literature and shown to be effective in similar situations^{55,56}. These algorithms define an acceptable threshold for a path to be executed and then create the route once a path is found that meets the threshold limit.

5.3 Limitation Testing

This section explains the input spaces of interest where the program may face serious bottlenecks or failures at the high level. The inputs used to test the Python3 simulation specify a random gene consisting of 5 symbols at the expected grid size of 1000 × 1000 gridpoints. When the input grid size exceeded this grid size the program’s runtime increased beyond practicality, taking over an hour to synthesize the gene routing about 30 droplets.

On the other hand, the program fails when grid sizes are small enough to generate considerable congestion. Within the context of the simulation, when the grid size becomes smaller than 40 × 40, given all other default parameters, there are issues with synthesis due to droplet congestion. A gene of length 5 pulls a total of 29 droplets as shown in Fig. 21, and all of these droplets need to be routed without causing collisions. In these situations, droplet paths may be blocked long enough to trigger a timeout where the synthesis of the gene is no longer pursued.

Aside from grid size, the number of reaction sites (Gibson, purification, PCR) can limit runtime and potentially cause timeout from congestion if very few of these sites exist on the chip. More-

over, there is a limited amount of chemistry sites the DMFB will allow due to its physical grid size. The number of reaction sites the DMFB contains depends on its physical grid size. Additionally, the number of reaction sites cannot exceed the number of possible reaction site locations.

5.4 Congestion Testing

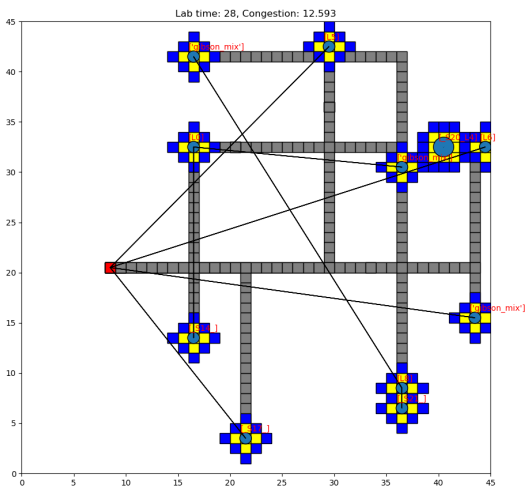


Fig. 20 Image of the simulation's GUI displaying droplets being routed in a 45×45 size grid at a gene length of 10 with additional droplet information visualization. The number of full command execution rounds and congestion are shown at the top as the lab time. Congestion is computed as the number of routed (grey), inhabited (yellow), and occluded (blue) gridpoints divided by the total number of gridpoints. The grey squares are included in congestion calculations as "no go" zones to avoid cross-droplet contamination as a droplet going through that zone may pick up debris from a previous droplet using that location. Congestion, in this sense, is a broad description of the simulated lab's congestion as a whole. Routed gridpoints are included in the calculation to indicate routing congestion for the prioritized 3-D A* algorithm.

Fig. 20 shows a visualization of multiple droplets being routed to one gibson site. The yellow squares represent the shadow of a droplet and the blue squares are their occlusion zones. We display the paths of various droplets shown as grey squares to indicate these as "no go" zones for other droplets. To other droplets, these grey squares are temporarily forbidden from crossing to avoid contamination of the droplet as it may pick up debris from a previously routed droplet, which is undesirable. Of course, this issue is hardware specific, but it is considered a constraint in our simulation and therefore contributes to congestion calculations.

The program can timeout under conditions of extreme congestion. This may occur for a number of input combinations, most notably when the grid size becomes too small. In these cases, there may be too few reaction sites, or too many droplets (as a consequence of synthesizing a long target gene). Any combination of these factors may lead to a situation where droplet paths are blocked and progress cannot be made. The simulation then times out and the synthesis of the target droplet is abandoned.

To analyze congestion the program was ran on a range of gene lengths two to twelve on a single machine (Machine 3 in Table 3) at a constant grid size (45×45). For each gene length the number of droplets pulled, the maximum number of concurrent droplets, and the grid's maximum congestion were recorded. Congestion is computed as the number of routed, inhabited, and occluded gridpoints divided by the total number of gridpoints. The number of droplets pulled is directly related to the length of the target gene. In Fig. 21 and Fig. 22, data points are labeled with their gene length for reference. As the total number of droplets increase (due to increasing gene length) the maximum number of concurrent droplets and maximum congestion increase linearly. Analyzing runtime again but in the context of congestion, as the number of total droplets pulled from reservoirs increases the runtime increases approximately exponentially (Fig. 23).

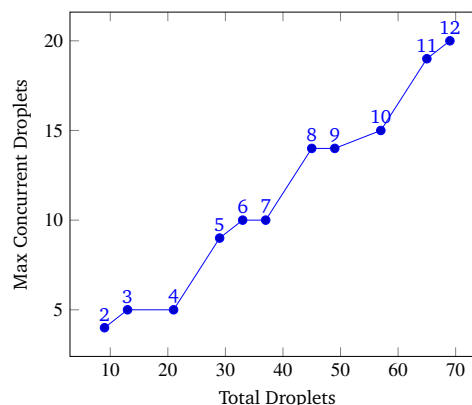


Fig. 21 Max Concurrent Droplets vs. Total Droplets. This data was obtained by running the simulation at a constant grid size of 45×45 over a range of gene lengths two to twelve. The number above each point represents the gene length. The vertical axis displays the maximum number of droplets recorded on the chip during the entirety of the simulation while the horizontal axis displays the total amount of droplets pulled from reservoirs to synthesize the gene. The relationship between the maximum number of active droplets and the number of total pulled droplets is approximately linear.

6 Conclusions

It is clear a new form of data storage is necessary to manage the worldwide increase in large scale information production. Current data storage centers cause environmental damage, and are unable to sustain the amount of data we generate. The rate of increase in data produced is growing too rapidly to continue using these data centers. Using DNA as a storage medium is the best option we have for its incomparable storage ability, environmental friendliness, and unmatched durability.

This paper proposes a solution to the DNA synthesis speed issue with a dual library of "Symbols" and "Linkers." We use this library in our system to perform automated DNA assembly on a virtual Digital Microfluidic Biochip. It presents a simulation displaying the proposed automated assembly of DNA, and the routing of droplets on a virtual lab grid.

When simulating droplet motion on a 1000×1000 grid, it was found that runtime was limited chiefly by CPU usage; al-

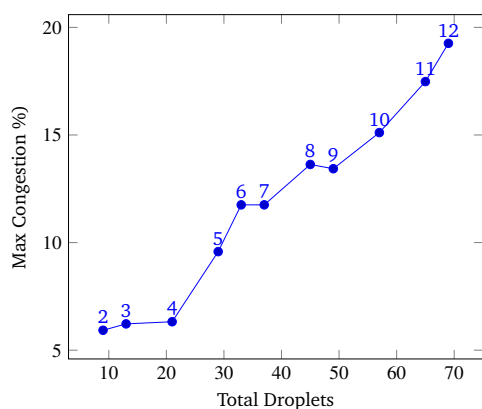


Fig. 22 Total Droplets vs. Max Congestion. This data was obtained by running the simulation at a constant grid size of 45×45 over a range of gene lengths two to twelve. The number above each point represents the gene length. The vertical axis displays the total congestion and the horizontal axis displays the total amount of droplets pulled from reservoirs to synthesize the gene. The relationship between the number pulled droplets and the maximum congestion is approximately linear.

though, we expect RAM usage to limit performance for very large grid sizes. In general, machines with higher specifications (faster CPUs and more RAM) yielded lower runtimes than machines with lower specifications. When grid size was swept from 500×500 to 1500×1500 , it was seen that runtime grew exponentially, RAM usage increased linearly, and CPU usage remained constant. The majority of runtime was spent advancing node instructions and moving droplets while the minority of time was spent routing droplets with the 3-D A* algorithm.

There is room for improvement in the system to apply different routing algorithms when the conditions for running this A* would cause significant congestion or timeout. The current algorithm seems ineffective at small grid sizes (less than 40×40) from droplet congestion, and exceedingly large grid sizes (greater than 1000×1000) as the rise in runtime begins to lose linearity and become exponential. The simulation must be parameterized with congestion in mind; factors such as grid size, number of reaction sites, and gene length influence grid congestion and consequently runtime. As the gene length was increased, the maximum number of concurrent droplets and maximum congestion increased linearly. These runtime results are specific to the simulated DMFB and do not take into account latencies which appear on physical boards. We note it is important to not compare runtime of our system to existing DNA storage technologies with physical implementations.

Writing complex genes will be commonplace when trying to store long chains of data. Therefore, an end-to-end system as proposed and simulated here is important to abstract the complexities away from the user and store information in a timely manner. This simulation can readily adapt to different gene lengths as it builds each gene from individual symbols and linkers.

It would be advantageous to incorporate algorithms which are better for memory management as peak RAM becomes the limiting factor for large grid sizes. Since algorithms like A* and Moving Target D* Lite are both heuristic based search algorithms,

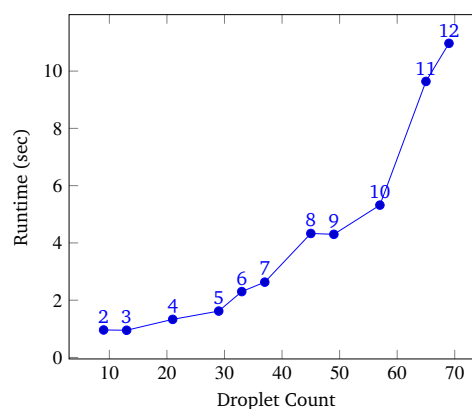


Fig. 23 Total Droplets vs. Runtime. This data was obtained by running the simulation at a constant grid size of 45×45 over a range of gene lengths two to twelve. The number above each point represents the gene length. The vertical axis displays the total congestion and the horizontal axis displays the runtime of the simulation. The relationship between the number pulled droplets and runtime is approximately exponential.

they will find the shortest path under given constraints. However, these algorithms do not consider the search time and memory requirements necessary to find such path. There exists a family of algorithms called Conflict Based Search (CBS) algorithms which help prune unnecessary branches of the search tree to manage memory and improve speed. It is known from previous work that algorithms like A* can become inefficient for large grid sizes leading to extremely large runtimes. Conflict based searching can be beneficial towards improving efficiency in problems involving multiagent path finding⁵⁷. In the problem surrounding routing many droplets on a DMFB, it may be useful to implement this CBS framework to maximize speed and minimize memory usage.

Future work will consist of introducing massive parallelization of the code. The platform we developed currently is written to only be used on one CPU thread, and it would be advantageous to split the work across multiple threads, especially when determining droplet routes with prioritized 3-D A*. The platform will also be migrated from Python3 to C++ in favor of the better optimization and data structure management.

There is room to optimize the code specifically by choosing a different routing algorithm. It is believed further testing can be executed to simulate more complex genes to evaluate its performance using the current prioritized A* algorithm against other competitive routing algorithms. One possibility for routing improvement includes using different multi-agent path planning touting faster speeds and area management than traditional A* heuristic search^{58,59}. Moreover, additional testing on input spaces to find optimal input combinations would be advantageous to defining the potential minimum runtime. While these changes are planned for future testing, this paper is a stepping stone towards realistically transforming modern storage media from current solid-state technologies to a DNA based platform.

Author Contributions

A. Manicka was the primary author of the manuscript as well as the project manager. A. Stephan was the software architect and

developer for the software system. S. Chari analyzed the computer science intensive sections of the manuscript. G. Mendonsa aided with the biochemistry background material described in the manuscript. P. Okubo conducted software testing on the system. J. Stolzberg-Schray described portions of the A* background section. A. Reddy and M. Riedel were the principal investigators for the project. All authors have contributed to the writing of this article.

Acknowledgements

We would like to thank Matthew Boros and Hershen Nair for comments and edits that greatly improved the quality of the manuscript.

Conflicts of interest

There are no conflicts to declare.

References

- 1 J. Li, R. J. Stones, G. Wang, X. Liu, Z. Li and M. Xu, *Reliability Engineering & System Safety*, 2017, **164**, 55–65.
- 2 IDC, *Worldwide Global DataSphere Forecast, 2021–2025: The World Keeps Creating More Data — Now, What Do We Do with It All?*, IDC Doc #US46410421, 2021.
- 3 C. Mellor, *Zettabyte era brings archiving front and center*, 2022, <https://blogsandfiles.com/2022/07/11/zettabyte-era-brings-archiving-front-and-center/>.
- 4 IDC, *Worldwide Global StorageSphere Forecast, 2021–2025: To Save or Not to Save Data, That Is the Question*, IDC Doc #US47509621, March 2021.
- 5 J. Monroe and R. Preston, *Gartner Inc., Market Trends: Evolving Enterprise Data Requirements — How Much Is Not Enough?*, July 2020.
- 6 E. Leproust, *Data Centers Are Unsustainable. We Need to Store Data in DNA*, 2022.
- 7 S. Greengard, *Communications of the ACM*, 2017, **60**, 16–18.
- 8 G. Church, Y. Gao and S. Kosuri, *Science (New York, N.Y.)*, 2012, **337**, 1628.
- 9 A. El-Shaikh, M. Welzel, D. Heider and B. Seeger, *NAR genomics and bioinformatics*, 2022, **4**, lqab126.
- 10 L. Ceze, J. Nivala and K. Strauss, *Nature Reviews Genetics*, 2019, **20**, 456–466.
- 11 J. D. Watson and F. H. Crick, *Cold Spring Harbor symposia on quantitative biology*, 1953, pp. 123–131.
- 12 K. Chen, J. Zhu, F. Bošković and U. F. Keyser, *Nano Letters*, 2020, **20**, 3754–3760.
- 13 G. D. Dickinson, G. M. Mortuza, W. Clay, L. Piantanida, C. M. Green, C. Watson, E. J. Hayden, T. Andersen, W. Kuang, E. Graugnard, R. Zadejan and W. L. Hughes, *Nature Communications*, 2021, **12**, 2371.
- 14 A. Mearns, K. Susumu, D. Mathur, S. H. Lee, O. A. Mass, J. Lee, R. D. Pensack, B. Yurke, W. B. Knowlton, J. S. Melinger *et al.*, *ACS omega*, 2022, **7**, 11002–11016.
- 15 M. Hepisuthar *et al.*, *Turkish Journal of Computer and Mathematics Education (TURCOMAT)*, 2021, **12**, 3635–3641.
- 16 Y. Erlich and D. Zielinski, *science*, 2017, **355**, 950–954.
- 17 E. Leproust, *Data Centers Are Unsustainable. We Need to Store Data in DNA*, 2022, Rev. 6.0.
- 18 W. Guo, S. Lian, C. Dong, Z. Chen and X. Huang, *ACM Transactions on Design Automation of Electronic Systems (TODAES)*, 2022, **27**, 1–33.
- 19 S. De Munter, A. Van Parys, L. Bral, J. Ingels, G. Goetgeluk, S. Bonte, M. Pille, L. Billiet, K. Weening, A. Verhee *et al.*, *International journal of molecular sciences*, 2020, **21**, 883.
- 20 I. M. Mackay, K. E. Arden and A. Nitsche, *Nucleic acids research*, 2002, **30**, 1292–1305.
- 21 E. R. Firmansyah, S. U. Masruroh and F. Fahrianto, 2016 6th International Conference on Information and Communication Technology for The Muslim World (ICT4M), 2016, pp. 275–280.
- 22 J. Yao, C. Lin, X. Xie, A. J. Wang and C.-C. Hung, 2010 Seventh international conference on information technology: new generations, 2010, pp. 1154–1158.

- 23 O. O. Martins, A. A. Adekunle, O. M. Olaniyan and B. O. Bolaji, *Scientific African*, 2022, **15**, e01068.
- 24 N. Goldman, P. Bertone, S. Chen, C. Dessimoz, E. M. LeProust, B. Sipos and E. Birney, *nature*, 2013, **494**, 77–80.
- 25 R. N. Grass, R. Heckel, M. Puddu, D. Paunescu and W. J. Stark, *Angewandte Chemie International Edition*, 2015, **54**, 2552–2555.
- 26 J. Bornholt, R. Lopez, D. M. Carmean, L. Ceze, G. Seelig and K. Strauss, *Proceedings of the Twenty-First International Conference on Architectural Support for Programming Languages and Operating Systems*, 2016, pp. 637–649.
- 27 M. Blawat, K. Gaedke, I. Huetter, X.-M. Chen, B. Turczyk, S. Inverso, B. W. Pruitt and G. M. Church, *Procedia Computer Science*, 2016, **80**, 1011–1022.
- 28 F. Su, W. Hwang and K. Chakrabarty, *Proceedings of the Design Automation & Test in Europe Conference*, 2006, pp. 1–6.
- 29 T. Xu and K. Chakrabarty, *proceedings of the 44th annual Design Automation Conference*, 2007, pp. 948–953.
- 30 Y. Zhao and K. Chakrabarty, *IEEE Transactions on Computer-Aided Design of Integrated Circuits and Systems*, 2012, **31**, 242–254.
- 31 C.-H. Liu, H.-H. Chang, T.-C. Liang and J.-D. Huang, 2013 IEEE/ACM International Conference on Computer-Aided Design (ICCAD), 2013, pp. 615–621.
- 32 S. J. Lehotay and J. M. Cook, *Journal of agricultural and food chemistry*, 2015, **63**, 4395–4404.
- 33 F. Perut, D. Dallari, N. Rani, N. Baldini and D. Granchi, *Current Pharmaceutical Biotechnology*, 2016, **17**, 1079–1088.
- 34 G.-R. Lu, C.-H. Kuo, K.-C. Chiang, A. Banerjee, B. B. Bhattacharya, T.-Y. Ho and H.-M. Chen, *ACM Transactions on Design Automation of Electronic Systems (TODAES)*, 2018, **23**, 1–25.
- 35 J. Juárez, C. A. Brizuela and I. M. Martínez-Pérez, *Information Sciences*, 2018, **429**, 130–146.
- 36 T.-C. Liang and Z. Zhong, *Proceedings of the 37th International Conference on Machine Learning*, 2020.
- 37 Y.-H. Chen, C.-L. Hsu, L.-C. Tsai, T.-W. Huang and T.-Y. Ho, *IEEE Transactions on Computer-Aided Design of Integrated Circuits and Systems*, 2013, **32**, 1151–1162.
- 38 N.-R. Shih and T.-Y. Ho, *Proceedings of the 26th Asia and South Pacific Design Automation Conference*, 2021, pp. 73–78.
- 39 K. Bohringer, *IEEE International Conference on Robotics and Automation*, 2004. *Proceedings. ICRA'04*. 2004, 2004, pp. 1468–1474.
- 40 H. Tsung-Wei and T. Ho, *IEEE International Conference on Computer Design*, 2009, pp. 445–450.
- 41 F. Mugele and J.-C. Baret, *Journal of physics: condensed matter*, 2005, **17**, R705.
- 42 R. B. Fair, *Microfluidics and Nanofluidics*, 2007, **3**, 245–281.
- 43 D. Millington, S. Norton, R. Singh, R. Sista, V. Srinivasan and V. Pamula, *Expert review of molecular diagnostics*, 2018, **18**, 701–712.
- 44 Y.-T. Yang and T.-Y. Ho, *Front. Chem.*, 2021, **9**, 676365.
- 45 H. Tegally, J. E. San, J. Giandhari and T. de Oliveira, *BMC Genomics*, 2020, **21**, 729.
- 46 B. F. Bender, A. P. Aijian and R. L. Garrell, *Lab on a Chip*, 2016, **16**, 1505–1513.
- 47 D. G. Gibson, L. Young, R.-Y. Chuang, J. C. Venter, C. A. Hutchison and H. O. Smith, *Nature methods*, 2009, **6**, 343–345.
- 48 R. Lopez, Y.-J. Chen, S. Dumas Ang, S. Yekhanin, K. Makarychev, M. Z. Racz, G. Seelig, K. Strauss and L. Ceze, *Nature communications*, 2019, **10**, 1–9.
- 49 Z. Zhang, J. Wu, J. Dai and C. He, *IEEE Access*, 2020, **8**, 122757–122771.
- 50 T.-W. Huang, C.-H. Lin and T.-Y. Ho, 2009 IEEE/ACM International Conference on Computer-Aided Design-Digest of Technical Papers, 2009, pp. 151–156.
- 51 X. Sun, W. Yeoh and S. Koenig, *Proceedings of the 9th International Conference on Autonomous Agents and Multiagent Systems: volume 1-Volume 1*, 2010, pp. 67–74.
- 52 Z. Hua, J. L. Rouse, A. E. Eckhardt, V. Srinivasan, V. K. Pamula, W. A. Schell, J. L. Benton, T. G. Mitchell and M. G. Pollack, *Analytical chemistry*, 2010, **82**, 2310–2316.
- 53 T. Loveless, J. Ott and P. Brisk, *Proceedings of the 18th ACM/IEEE International Symposium on Code Generation and Optimization*, 2020, pp. 171–184.
- 54 *Passmark Support*, https://www.passmark.com/support/performance_test_faq/understanding_results.php.
- 55 Y. Liu and L. Zhu, 2018 International Symposium on Networks, Computers and Communications (ISNCC), 2018, pp. 1–5.
- 56 S. Katoch, S. S. Chauhan and V. Kumar, *Multimedia Tools and Applications*, 2021, **80**, 8091–8126.
- 57 Z. Ren, S. Rathinam and H. Choset, *IEEE Transactions on Automation Science and Engineering*, 2022.
- 58 J. Li, Z. Chen, D. Harabor, P. J. Stuckey and S. Koenig, *Proceedings of the AAAI Conference on Artificial Intelligence*, 2022.
- 59 P. Pianpak and T. C. Son, *arXiv preprint arXiv:2109.08288*, 2021.